Proceedings of the 21st ICSMGE, Vienna, Austria, 14 – 19 June 2026. Pistrol, Adam & Schweiger (eds.)
Published by: ÖGG, Austrian Society for Geomechanics, Salzburg, Austria, ISBN 978-3-9503898-4-5
https://doi.org/10.53243/ICSMGE2026-2107

High-resolution microCT analysis of porosity and permeability in deep soil mixing (DSM) columns: a framework for material optimization and performance verification

Michał Pachnicz
Faculty of Civil Engineering, Wroclaw University of Science and Technology, Wrocław, Poland
michal.pachnicz@pwr.edu.pl

Jarosław Rybak
Faculty of Civil Engineering, Wrocław University of Environmental and Life Sciences, Wrocław, Poland

Piotr Kanty
MENARD Polska Sp. z o.o. ul. Powązkowska 44c, 01-797 Warsaw, Poland

ABSTRACT: The permeability of Deep Soil Mixing (DSM) columns is a key parameter in the performance of impermeable barriers for geotechnical and environmental applications. This study applies high-resolution X-ray microcomputed tomography (microCT, voxel size 20 μm) to characterize the microstructure of DSM materials prepared with varying cement contents and water-to-cement ratios. Analyses focused on the pore phase and a combined phase encompassing both pores and weakly cemented zones (WZ). Quantitative metrics included volumetric fractions, morphology, and tortuosity, with the latter used to estimate hydraulic conductivity via Kozeny–Carman and surface-density-based models. Results show that in many samples the pore phase alone is poorly connected or non-percolating, whereas WZ substantially increases connectivity and reduces tortuosity, leading to higher estimated hydraulic conductivity. While this approach treats WZ as hydraulically equivalent to open pores, their intrinsic permeability is likely lower, representing an important subject for further research. The study demonstrates that microCT provides a robust, non-destructive framework for linking DSM microstructure to permeability performance and guiding mix design to minimize continuous low-density pathways.

KEYWORDS: Deep Soil Mixing (DSM), microCT, tortuosity, hydraulic conductivity.

1 INTRODUCTION

Deep Soil Mixing (DSM) is a widely adopted in-situ soil improvement technique in which native soil is mechanically blended with a cementitious slurry to form soil–cement columns with enhanced strength and reduced permeability(Polańska and Rybak, 2020). Beyond its common use for ground stabilization, DSM is also increasingly applied to form cut-off walls and impervious barriers in geotechnical and hydraulic engineering works, such as flood protection embankments, landfill containment systems, or groundwater pollution control projects. The key performance criterion in such sealing applications is achieving a low hydraulic conductivity and long-term durability under varying hydrogeological conditions.

Despite technological advancements in mixing equipment and quality control procedures, DSM columns inherently exhibit heterogeneity arising from the execution process. This heterogeneity occurs at two distinct scales. At the macroscale, inhomogeneity may result from stratigraphic variability of the treated soil, such as thin interbedded layers, coarse gravel lenses, or isolated rock fragments. While such large-scale variability is challenging to eliminate entirely, careful adjustment of execution parameters (e.g., mixing energy, slurry feed rate) can reduce its influence, often yielding a macroscopically uniform barrier. At the microscale, heterogeneity is related to the spatial distribution and interaction between soil grains and the cementitious binder, as well as the microstructural evolution of the cement matrix during curing. This level of heterogeneity is more directly controllable through mix design optimization, including cement content, water-to-cement ratio (w/c), and potential admixtures. Importantly, both scales of inhomogeneity can form preferential filtration pathways, thereby increasing the permeability of the barrier. Even when a DSM wall appears macroscopically uniform, its material may still permit water seepage through micropores or microcracks within the cement matrix.

In the context of cement-based composites, microCT enables not only quantification of total porosity but also assessment of pore connectivity, morphology, and spatial distribution of zones with reduced binder density. These capabilities make microCT particularly suitable for investigating microstructural causes of permeability in DSM materials, bridging the gap between conventional macroscale permeability tests and the underlying pore-scale mechanisms.

Previous microCT studies have focused on cementitious materials such as mortars, concretes, or soil–cement composites prepared in laboratory conditions, but few have addressed the specific challenges of DSM barriers (Chung et al., 2019). Existing work has typically evaluated porosity in isolated terms, without fully integrating the role of weakly cemented zones—regions of the cement matrix with high microporosity and low binder density—into permeability assessment (Amrioui et al., 2023). This omission is significant, as both open pores and weakly cemented zones can form hydraulically relevant pathways.

This study proposes a methodological framework for using microCT to assess microstructural features relevant to the hydraulic performance of DSM materials. For the analyzed materials total porosity, the fraction of open versus closed pores, as well as the volume fraction of weakly cemented zones were quantified. Importantly, tortuosity was computed for a combined phase comprising both open pores and weakly cemented zones, representing potential continuous filtration pathways. Additional morphological parameters—including local feature size, shape descriptors, and connectivity—were also derived.

The findings aim to demonstrate that high-resolution microCT not only provides accurate porosity and connectivity measurements but also offers insight into the openness and morphology of potential seepage pathways. This approach supports rational mix design optimization for DSM barriers,

with the broader potential to assess the effect of admixtures such as plasticizers or nanoparticles in future work.

2 MATERIALS AND METHODS

2.1 *Materials*

The soil–cement composites investigated in this study were prepared by mixing a field sampled sand with a cement slurry. Ordinary Portland cement (CEM I 42.5R) was used as the binder. The idea of the work was to evaluate possible benefits of using higher density of the binding cement slurry. Four series of mixtures were designed to represent both: typical ranges of cement dosage and water-to-cement ratios (w/c) used in DSM cut-off wall construction and mixtures with low w/c (higher density) that represented perspective progress in the technology. Cement dosages of 300, 340, and 265 kg/m³ (per unit volume of the final composite) were selected, combined with w/c ratios ranging from 0.40 to 1.33 Table 1. These parameters yielded slurries of different densities and viscosities, which are expected to influence the microstructural development of the hardened material. For each sample, the bulk density of the fresh mixture ρ_w and the bulk density after curing (28 days) ρ_c were determined.

Table 1. Mix design and density parameters for the analyzed DSM sample series

Sample series	Water to cement ratio w/c	Slurry density ρ [t/m³]	Cement dosage [kg/m³]	ρ_w [t/m³]	ρ_c [t/m³]
1A	0.89	1.45	300	2.12	2.05
1B	0.81	1.50	300	2.17	2.11
2A	0.56	1.75	300	2.12	2.09
2B	0.40	2.08	300	2.11	2.06
3A	0.56	1.75	340	2.12	2.08
3B	0.68	1.60	340	2.17	2.10
4A	0.89	1.45	265	2.17	2.11
4B	1.33	1.35	265	2.18	2.08

2.2 *Sample preparation*

From the cured specimens of each series, a rectangular fragment measuring approximately 20 mm × 20 mm × 40 mm was cut for microCT analysis. Cutting was performed using a Struers Labotom 5 precision cut-off saw equipped with isopropanol cooling to prevent thermal damage to the cement matrix. Subsequently, the specimens were ground to the final dimensions of 10 mm × 10 mm × 30 mm using SiC abrasive wheels, applying gentle manual pressure and continuous isopropanol cooling to minimize microcracking and edge chipping. The prepared sample surfaces were cleaned with compressed air to remove any residual abrasive particles or debris. Finally, all specimens were placed in a desiccator and left to dry for 72 h prior to scanning to ensure removal of free moisture.

2.3 *MicroCT acquisition and reconstruction*

High-resolution X-ray micro-computed tomography was conducted using a GE Phoenix v|tome|x s system equipped with a DXR-250 RT detector (1000 × 1000 pixels, 16-bit depth). The scans were acquired at an accelerating voltage of 70 kV and a tube current of 140 µA, with an effective focal spot size of approximately 9.8 µm. The source-to-object and source-to-detector distances were set to 81.41 mm and 813.94 mm, respectively, yielding a geometric magnification close to 10× and an isotropic voxel size of 20 µm. A total of 1500 projections were recorded over a full 360° rotation, with an exposure time of 500 ms per projection and frame averaging to enhance signal-to-noise ratio.

Reconstruction was performed in datos|x 2.6.1 using a Feldkamp filtered back-projection algorithm(Feldkamp, Davis and Kress, 1984). A cubic voxel size of 20 µm was maintained, and the region of interest was cropped to 700 × 700 × 800 voxels to focus on the central volume free of edge artefacts.

2.4 *Image processing and phase segmentation*

Prior to segmentation, the grayscale intensity range of each reconstructed dataset was normalized to a common reference scale, ensuring comparability of voxel intensity values between specimens. This step was essential for subsequent quantitative analysis, as the reconstructed attenuation coefficient (γ_{rec}) is directly related to the local material density and must be consistent across all samples. From each reconstructed volume, a volume of interest (VOI) measuring 8 × 8 × 16 mm was extracted from the central region of the specimen to avoid edge artefacts. Within this VOI, the distribution of γ_{rec} was evaluated to qualitatively and quantitatively assess material density variations (Figure 1).

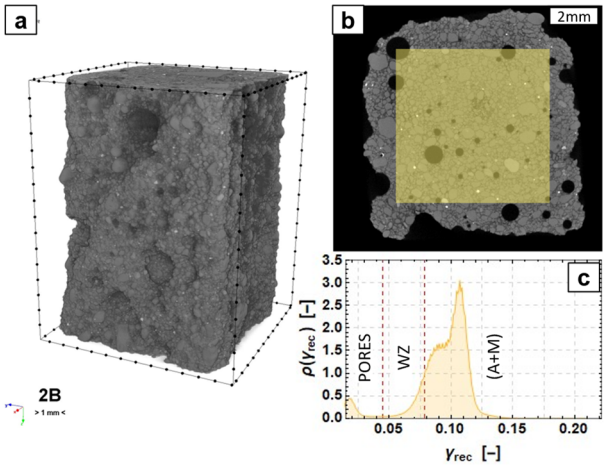

Figure 1. Example of a reconstructed volume (a) with the ROI presented for selected slice (b), with the corresponding normalized grayscale histogram and identified threshold levels (c) for sample 2B.

Segmentation of material phases was carried out in Bruker CTAn 1.20.8. A 3D unsharp masking filter (radius = 2 voxels, amount = 50%) was applied to enhance phase boundaries. The VOI was then segmented into three distinct phases (Figure 2):

- Pore space – representing air-filled or void regions,
- Weakly cemented zones (WZ) – regions of cement matrix with reduced grayscale intensity, indicative of higher microporosity or incomplete binder densification,
- Aggregate and dense cement matrix (A+M) – encompassing sand grains and well-hydrated cement paste.

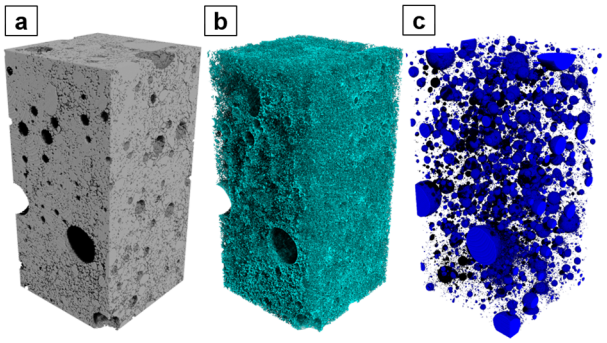

Figure 2. 3D rendering of segmented phases for sample 2B: (a) aggregate and dense cement matrix, (b) weakly cemented zones, (c) pore space.

Segmentation was performed using the Multilevel Otsu algorithm with five threshold levels applied to the normalized grayscale histogram. Threshold boundaries were determined automatically and verified through visual inspection of orthogonal slices and 3D renderings to ensure correct phase attribution.

For subsequent hydraulic pathway analysis, the pore phase and WZ phase were merged into a single combined phase, representing the interconnected microstructural features most likely to facilitate seepage. This combined phase served as the basis for connectivity, morphological, and tortuosity analyses.

2.5 *Quantitative microstructural metrics*

Quantitative characterization of the internal microstructure was performed on the segmented volumes of interest (VOIs) described in Section 2.4. All analyses were conducted on the combined filtration pathway phase, comprising both the pore space and weakly cemented zones (WZ), as well as on the individual pore phase when indicated. This approach reflects the hydraulic relevance of both macropores and microporous low-density binder regions in DSM materials.

2.5.1 *Total porosity and phase volume fractions*

Total porosity (ϕ_{total}) was calculated as the ratio of the binarized pore volume (V_p) to the total VOI volume (V_{tot}). For comparative purposes, the volume fraction of WZ and of the dense aggregate–cement matrix phase were also computed.

2.5.2 *Partitioning of open and closed porosity*

Open and closed porosity were distinguished using a 3D connectivity analysis in Bruker CTAn, applying a shrink-wrap region of interest tightly enclosing the material. Pores connected to both the top and bottom faces of the VOI were classified as open porosity, representing potential continuous seepage channels. All remaining voids, including isolated cavities and partially connected clusters, were classified as closed porosity. This classification was also applied to the combined phase to identify open filtration pathways formed jointly by pores and WZ regions.

2.5.3 *Morphological analysis*

Morphometric descriptors were extracted to quantify the size, shape, and surface complexity of the identified phases:

- Local thickness (StTh) / Pore width (D) – Calculated as the diameter of the largest sphere that can be inscribed at each point within the pore or combined phase, using a 3D distance transform.
- Object surface density (S) – Defined as the total internal surface area of the segmented phase per unit volume of the VOI. This parameter reflects the extent and complexity of the interface between the filtration pathway phase and the surrounding dense matrix.

$$S = \frac{A_{pore}}{V_{tot}} \quad [mm^{-1}], \qquad (1)$$

- Structure Model Index (SMI) – A dimensionless measure of the predominant 3D geometry of the phase, ranging from 0 for plate-like structures to 3 for cylindrical rods and 4 for spherical cavities. Negative values correspond to concave or enclosed morphologies. In the context of DSM materials, higher SMI values for open pathways may indicate channel-like connectivity, whereas lower values reflect more laminar or sheet-like features.

$$SMI = 6\frac{EV\frac{dS}{dr}}{ES^2} \quad [-], \qquad (2)$$

where: dS/dr is the derivative of the external surface S of the element (pores, i.e. the area of cracks) after the size of its hypothetical expansion joint r, EV – the volume of the element, ES – the external surface of the element.

2.5.4 *Tortuosity analysis*

Tortuosity (τ) was calculated for the combined filtration pathway phase using a 3D geodesic dilation approach. Two seed masks were placed at opposite faces of the VOI along the presumed hydraulic gradient (Z-axis).

Iterative dilation within the connected phase recorded the number of voxel layers traversed from each face, allowing the calculation of the actual path length relative to the geometric specimen height. Voxel-wise tortuosity values were aggregated to produce mean, minimum, and maximum τ statistics. Values close to 1 represent nearly straight, low-resistance pathways, while higher values indicate convoluted flow paths with potentially higher hydraulic resistance.

2.5.5 *Permeability estimation*

Although microCT does not directly measure fluid flow, the extracted microstructural parameters were used to estimate intrinsic permeability (k) via semi-empirical relationships such as the Kozeny–Carman equation (Kozeny, 1927), or the one proposed by Xu and Yu, (2008). In addition, knowing the relationship between permeability and hydraulic conductivity:

$$k == \frac{\gamma_w}{\mu} \cdot K, \qquad (3)$$

where: γ_w=9.8 kN/m^3 – water unit weight, μ=1.0e-3 Pa s – dynamic viscosity of water,

one can calculate the hydraulic conductivity from the following relations:

$$k = \frac{\gamma_w}{\mu} \cdot \frac{\phi D^2}{32\tau^2}, \qquad (4)$$

$$k = \frac{\gamma_w}{\mu} \cdot \frac{\phi^3}{c \cdot \tau^2 \cdot (1-\phi)^2 \cdot S^2}, \qquad (5)$$

where: ϕ – porosity, D – pore width, τ – tortuosity, S – object surface density, c – constant, equal to approx. 2.15.

3 RESULTS

3.1 *Microstructural visualization*

The parameter γ_{rec}, directly derived from the X-ray attenuation in the reconstructed volumes, is indicative of local material density and, indirectly, of binder compaction and homogeneity. Figure 3 shows the overlaid histograms of γ_{rec} distributions for all analyzed samples.

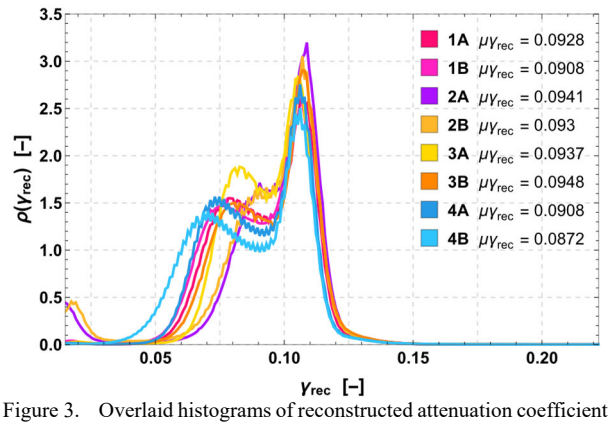

Figure 3. Overlaid histograms of reconstructed attenuation coefficient (γ_{rec}) for all DSM samples, with mean values indicated in the legend. Differences in mean γ_{rec} and distribution width reflect variations in density and microstructural uniformity between series.

Despite the similar overall shape of the histograms, distinct differences in the mean γ_{rec} values can be observed between series. Samples with higher mean γ_{rec} tend to exhibit a denser and more uniform cement matrix, while lower mean values suggest a greater proportion of microporous regions or incomplete binder hydration. The variability in histogram peak width further reflects differences in microstructural uniformity—narrow peaks correspond to more homogeneous microstructures, whereas broader peaks indicate higher density heterogeneity.

To illustrate the microstructural implications of these differences, Figure 4 presents representative cross-sections for two specimens with the largest contrast in mean γ_{rec}: one from the high-density group (e.g., Series 3B) and one from the low-density group (e.g., Series 4B). The segmented images highlight the spatial distribution of the three phases, with particular emphasis on the connectivity of pore space and WZ. In the low- γ_{rec} sample, pores are more abundant and often form partially connected clusters, whereas in the high- γ_{rec} sample, they are sparse and more uniformly dispersed.

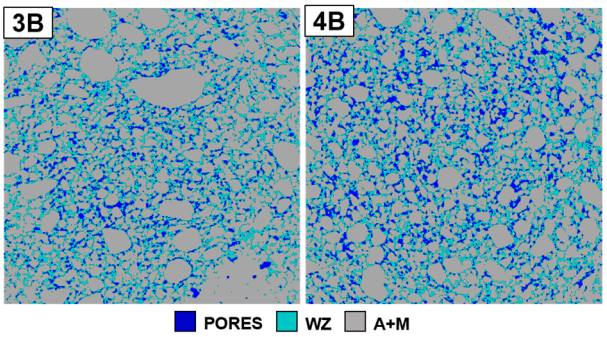

Figure 4. Representative cross-sections of segmented phases for specimens with high (3B) and low (4B) mean γ_{rec}.

In the denser material, exemplified by sample 3B, the segmented images reveal a larger fraction of well-cemented matrix. This phase is more continuous and frequently forms extended clusters together with sand grains, resulting in a compact and interconnected solid skeleton.

In both specimens, the morphology of the weakly cemented zones (WZ) is similar—these regions tend to develop adjacent to pore space and along the interfaces with aggregate particles. However, in the lower-density sample 4B, WZ regions are more volumetrically continuous, often forming elongated or interconnected patterns that can link multiple pores. This difference in spatial continuity is consistent with the lower mean γ_{rec} value and the broader histogram distribution observed for this specimen.

3.2 *Porosity, WZ, and connectivity of potential filtration pathways*

For each phase, the morphometric descriptors described in Section 2.5 were also calculated, including structure thickness (StTh), surface density (S), and structure model index (SMI). The results for the pore phase are summarized in Table 2, while those for the combined phase are presented in Table 3.

For the pore phase, volumetric fractions ranged from 0.75% (3A) to 11.01% (4A), with open pore networks absent in several samples (1B, 2A, 2B, 3A). In cases where open pores were present, their fraction often represented the majority of the total pore volume - as in 4A and 4B, where over 75% of the pore space formed continuous pathways. Structure thickness values were generally low (<0.12 mm) for samples with high open porosity, while isolated large voids in samples such as 2A and 2B resulted in elevated StTh (>0.5 mm) despite the absence of connectivity. SMI values in connected pore systems were close to 2, indicating cylindrical or channel-like geometries, whereas high SMI in closed systems reflected more complex enclosed morphologies.

Table 2. Quantitative microstructural parameters for the pore phase in DSM samples.

Porosity					
Sample	**Fraction type**	**φ** [%]	**StTh** [mm]	**S** [1/mm]	**SMI** [-]
1A	Total	8.561	0.077	9.705	2.340
	Open	4.485	0.112	4.144	1.963
1B	Total	7.884	0.078	8.907	2.464
	Open	0.000	--	--	--
2A	Total	6.494	1.572	0.568	16.413
	Open	0.000	--	--	--
2B	Total	6.579	0.792	0.882	10.943
	Open	0.000	--	--	--
3A	Total	0.750	0.242	0.464	6.805
	Open	0.000	--	--	--
3B	Total	7.306	0.058	8.263	2.441
	Open	2.846	0.071	2.628	2.044
4A	Total	11.008	0.056	11.827	2.069
	Open	8.606	0.060	8.331	1.851
4B	Total	9.986	0.048	10.506	2.187
	Open	7.024	0.049	6.508	1.854

Table 3. Quantitative microstructural parameters for the combined phase (pore space + weakly cemented zones) in DSM samples.

Porosity + WZ					
Sample	**Fraction type**	**φ** [%]	**StTh** [mm]	**S** [1/mm]	**SMI** [-]
1A	Total	31.185	0.072	18.899	0.684
	Open	31.084	0.073	18.675	0.647
1B	Total	30.580	0.071	18.564	0.747
	Open	30.509	0.072	18.396	0.724
2A	Total	20.058	0.548	12.794	2.736
	Open	18.442	0.601	10.354	2.374
2B	Total	20.516	0.308	12.632	2.679
	Open	18.919	0.335	10.282	2.263
3A	Total	20.557	0.060	17.003	1.500
	Open	19.941	0.061	15.896	1.380
3B	Total	29.857	0.066	17.766	0.664
	Open	29.775	0.067	17.585	0.632
4A	Total	34.101	0.070	18.354	0.218
	Open	34.069	0.070	18.260	0.209
4B	Total	33.462	0.067	18.312	0.351
	Open	33.398	0.067	18.169	0.333

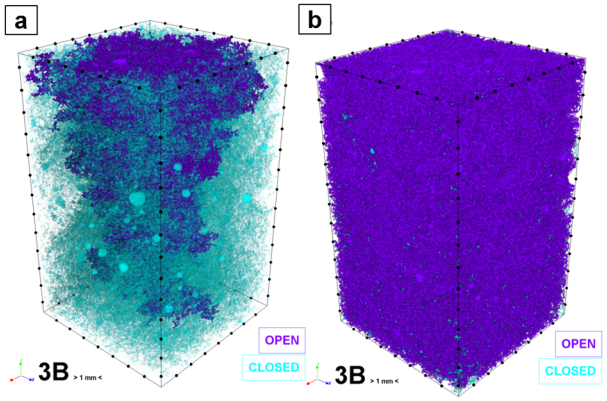

Figure 5. Three-dimensional renderings of open (purple) and closed (blue) phases for sample 3B: (a) pore phase only, showing a limited number of continuous pathways, and (b) combined phase (pores + WZ), revealing a dense and highly connected open network.

For the combined phase, volumetric fractions were markedly higher, ranging from ~20% in 2A–3A to over 34% in 4A. The difference between total and open fractions was minimal (<1% in all cases), showing that WZ regions are typically continuous and well connected to the pore network. Surface density values

for the combined phase were consistently higher than for pores alone, reflecting the additional internal surfaces contributed by WZ. SMI values for the combined phase were low (0.2–0.75), indicating more plate-like morphologies—consistent with WZ forming along pore walls and grain boundaries rather than as discrete cavities.

To illustrate the effect of including weakly cemented zones (WZ) in the connectivity analysis, Figure 5 presents 3D renderings of open and closed phases for sample 3B. In the pore phase alone, the open fraction is present but limited, forming only a few continuous pathways. When WZ are included, the open phase fraction increases more than six-fold, and a dense, interconnected network emerges. This comparison visually demonstrates the decisive role of WZ in extending and linking pore pathways within the microstructure.

3.3 *Tortuosity of filtration pathways and DSM hydraulic conductivity*

The spatial complexity of potential filtration pathways in DSM materials was quantified through tortuosity analysis, performed separately for the pore phase and the combined phase (pores + WZ). For each sample, the minimum (τ_{min}), mean (τ_{mean}), and maximum (τ_{max}) tortuosity values were determined. The mean value was then used in conjunction with porosity and morphological parameters (Section 2.5) to estimate the hydraulic conductivity (k) (Table 4).

Table 4. Tortuosity statistics and estimated hydraulic conductivity for pore and combined phases in DSM samples.

Sample	Fraction	τ_{mean} [-]	τ_{min} [-]	τ_{max} [-]	k (Eq. 4) [m/s]	k (Eq. 5) [m/s]
1A	Pores	2.318	1.710	4.420	3.20E-08	4.88E-09
	Comb.	1.338	1.190	2.270	2.84E-07	4.61E-07
1B	Pores	-	-	-	-	-
	Comb.	1.376	1.230	1.900	2.54E-07	4.18E-07
2A	Pores	-	-	-	-	-
	Comb.	1.835	1.405	3.785	6.06E-06	1.19E-07
2B	Pores	-	-	-	-	-
	Comb.	1.836	1.450	3.365	1.93E-06	1.32E-07
3A	Pores	-	-	-	-	-
	Comb.	1.645	1.295	3.415	8.38E-08	8.24E-08
3B	Pores	2.957	1.590	8.290	4.99E-09	1.84E-09
	Comb.	1.355	1.225	2.235	2.20E-07	4.30E-07
4A	Pores	2.960	2.240	6.250	1.08E-08	5.72E-09
	Comb.	1.342	1.235	1.750	2.86E-07	6.90E-07
4B	Pores	2.956	2.247	6.161	6.02E-09	4.94E-09
	Comb.	1.340	1.235	1.725	2.59E-07	6.45E-07

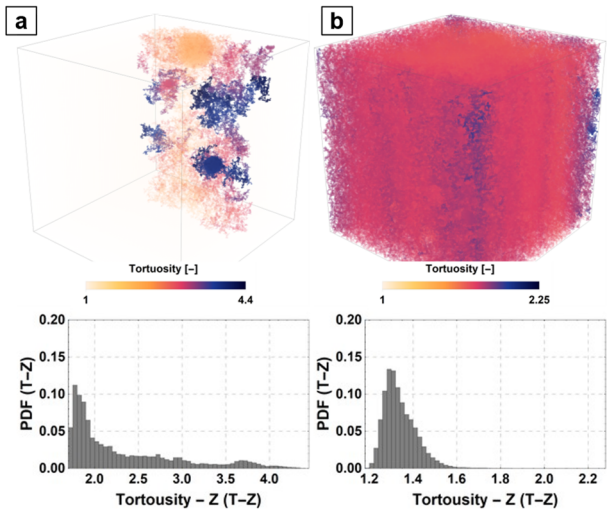

Figure 6. Spatial maps and histograms of tortuosity in the Z-direction for 1A sample: (a) pore phase only, and (b) combined phase (pores + WZ).

Figure 6 compares the spatial distribution of tortuosity values in the pore phase (a) and in the combined phase including both pores and weakly cemented zones (b) for a representative DSM specimen (1A). In the pore phase, high tortuosity values (>3) are locally concentrated along isolated, convoluted pathways, while large portions of the microstructure remain inaccessible to continuous flow. When WZ are included, the open-phase network becomes more uniformly connected, and the majority of pathways exhibit lower tortuosity values ($\tau \approx 1.3–1.6$), indicative of straighter and hydraulically more efficient channels. The corresponding histograms quantify these differences, showing a broader and right-skewed distribution for the pore phase, and a narrower, more symmetric distribution for the combined phase.

While τ_{min} and τ_{max} provide insight into the variability of local transport conditions within the microstructure, τ_{mean} offers the most representative metric for macroscale hydraulic behavior and is therefore applied in the permeability estimation.

For the pore phase, τ_{mean} values were generally higher (2.32–2.96) than for the combined phase (1.340–1.836), indicating a more convoluted and less direct connectivity of the pure pore network. This was especially evident in samples such as 3B and 4A, where τ_{mean} for pores approached 3, while the inclusion of WZ reduced tortuosity to ~1.35, reflecting straighter and more hydraulically efficient pathways.

It should be noted that the hydraulic conductivity estimates for the combined phase implicitly assume that water flow through weakly cemented zones is as efficient as through fully open pores. In practice, the microporous structure of WZ can significantly reduce local permeability due to smaller pore throats, higher surface area, and partial blockage by hydration products. This limitation is recognised as a subject for further study and will be addressed in the continuation of the present research.

4 DISCUSSION

4.1 *Microstructure–permeability relationships*

The results of the microstructural analyses demonstrate a direct link between the geometry and connectivity of the microstructural phases in DSM materials and their estimated hydraulic conductivity. Pore-phase data (Section 3.2) revealed that, in many samples, open porosity is either absent or forms only a small fraction of the total pore volume. This limited connectivity is reflected in the high mean tortuosity values ($\tau_{mean} > 2.3$) and low calculated k (as low as 10^{-9} m/s in dense matrices such as 3B).

The inclusion of weakly cemented zones (WZ) in the analysis fundamentally changes the connectivity landscape. In specimens with negligible open pore content (e.g., 1B, 2A, 2B, 3A, 4B), the combined phase becomes the sole continuous network, reducing mean tortuosity to 1.34–1.84 and increasing estimated k by one to two orders of magnitude.

However, the enhanced connectivity of the combined phase must be interpreted with caution. The current permeability estimates assume that water flow through WZ is as efficient as through fully open pores, whereas in reality, their microporous nature likely imposes a higher hydraulic resistance. This implies that the calculated k values for the combined phase represent an upper bound rather than an exact prediction of field performance. The morphological metrics support these observations: higher surface density (S) and lower SMI in the combined phase indicate more extensive, wall-adjacent, and plate-like structures compared to the more cylindrical geometry of the pore phase. Such geometries can enhance capillary retention and reduce flow efficiency, even if connectivity is high.

Overall, the interplay between low volumetric pore fractions, high tortuosity, and the bridging role of WZ highlights the need for permeability assessments that integrate both geometric connectivity and intrinsic phase permeability. This microstructural perspective not only explains the wide range of estimated *k* values but also provides a framework for targeted mix design adjustments aimed at minimizing continuous WZ networks and thereby reducing seepage potential.

4.2 *Material optimization guidelines*

The microstructural and permeability analyses provide a clear basis for optimizing DSM mix design to minimize the formation of continuous filtration pathways. Three main factors emerge as critical:

- Cement content – Higher cement dosage is consistently associated with lower volumetric fractions of WZ and reduced combined-phase connectivity. For example, in Series 3B (high cement, low w/c), the combined phase exhibited low volumetric fraction and tortuosity close to 1.35, but the overall permeability was significantly lower due to the reduced extent of connected low-density regions. This suggests that ensuring sufficient binder volume to fully encapsulate aggregate surfaces and pore walls is key to limiting WZ development.
- Water-to-cement ratio (w/c) – Elevated w/c ratios lead to higher WZ content and, consequently, higher connectivity of the combined phase. In samples such as 4B, the combined phase formed an almost fully connected network, resulting in high estimated *k* despite moderate total porosity. Optimization should therefore aim to avoid excessively high w/c values, which promote segregation and microstructural heterogeneity during curing.
- Microstructural uniformity – Histogram analysis of γ_{rec} revealed that narrower distributions correlate with denser, more uniform matrices and lower combined-phase fractions. This observation supports the use of additives (e.g., plasticizers, nano-silica) to improve slurry workability and packing density without increasing w/c ratio.

From a design perspective, the optimal strategy is to combine moderate to high cement content with controlled w/c ratio, targeting a microstructure in which WZ are either absent or remain short, isolated, and unconnected. Field performance could be further improved by applying admixtures that refine pore structure and reduce capillary porosity.

By embedding microCT-derived metrics into the design workflow, DSM mix optimization can move beyond empirical guidelines to a microstructure-driven approach. Such integration would allow engineers to set quantitative thresholds for WZ content, pore connectivity, and tortuosity, and thus design barriers with reliably low permeability while maintaining constructability in field conditions.

5 CONCLUSIONS

This study demonstrates the capability of high-resolution X-ray microcomputed tomography (microCT) to quantitatively characterize the microstructure of Deep Soil Mixing (DSM) materials and relate it directly to estimated hydraulic performance. By analyzing both the pore phase and a combined phase encompassing pores and weakly cemented zones (WZ), the work provides new insights into the role of WZ in defining permeability pathways within DSM barriers.

The main conclusions are:

(i) In many DSM specimens, the pore phase alone is poorly connected or entirely non-percolating, indicating limited direct seepage potential through open voids.

(ii) WZ substantially increases phase connectivity and reduces tortuosity, forming continuous plate-like structures along pore walls and aggregate contacts that can bridge isolated pores. The inclusion of WZ in the analysis increases estimated hydraulic conductivity by up to two orders of magnitude compared to the pore phase alone, highlighting their dominant role in seepage potential.

(iii) Mix composition strongly influences permeability: higher cement content and lower water-to-cement ratio reduce the volumetric fraction and connectivity of WZ, resulting in lower estimated hydraulic conductivity. Conversely, high w/c ratios promote WZ formation and increase the likelihood of continuous filtration pathways.

(iv) MicroCT-derived metrics, including volumetric fractions, morphological descriptors, and tortuosity, offer a robust, non-destructive basis for optimizing DSM mix design to minimize continuous low-density regions and improve barrier performance.

By integrating advanced microstructural characterization into the design and evaluation of DSM materials, this work strengthens the link between soil mechanics principles and micro-scale material behavior, contributing to more reliable and durable impermeable barriers in geotechnical engineering practice.

6 REFERENCES

Amrioui, J., Le Kouby, A., Duc, M., Guedon, J.-S. and Lansac, F., 2023. Relationship between Porosity and Water Permeability for Deep Soil Mixing Material. *International Journal of Geomechanics*, 23(7), p.04023086. https://doi.org/10.1061/IJGNAI.GMENG-8447.

Chung, S.-Y., Kim, J.-S., Stephan, D. and Han, T.-S., 2019. Overview of the use of micro-computed tomography (micro-CT) to investigate the relation between the material characteristics and properties of cement-based materials. *Construction and Building Materials*, 229, p.116843. https://doi.org/10.1016/j.conbuildmat.2019.116843.

Feldkamp, L.A., Davis, L.C. and Kress, J.W., 1984. Practical cone-beam algorithm. *Journal of the Optical Society of America A*, 1(6), p.612. https://doi.org/10.1364/JOSAA.1.000612.

Kozeny, J., 1927. Ueber kapillare leitung des wassers im boden. *Sitzungsberichte der Akademie der Wissenschaften in Wien*, 136, p.271.

Polańska, B. and Rybak, J., 2020. Barriers of Low Permeability to Water–Technical Solutions. In: *IOP Conference Series: Materials Science and Engineering*. [online] IOP Publishing. p.012219. Available at: <https://iopscience.iop.org/article/10.1088/1757-899X/883/1/012219/meta> [Accessed 14 August 2025].

Xu, P. and Yu, B., 2008. Developing a new form of permeability and Kozeny–Carman constant for homogeneous porous media by means of fractal geometry. *Advances in water resources*, 31(1), pp.74–81.